Originally published as:

Tanaka, Y., Sato, T., Ohta, Y., Miura, S., Freymueller, J. T., Klemann, V. (2015): The effects of compressibility on the GIA in southeast Alaska. - *Journal of Geodynamics*, *84*, p. 55-61.

DOI: http://doi.org/10.1016/j.jog.2014.10.001

The effects of compressibility on the GIA in southeast Alaska

Yoshiyuki Tanaka*

Earthquake Research Institute, University of Tokyo, 1-1-1 Yayoi, Bunkyo-ku, Tokyo 113-0032

Tadahiro Sato, Yusaku Ohta, Satoshi Miura

Research Center for Prediction of Earthquakes and Volcanic Eruptions, Tohoku University, 6-6 Aoba, Aramaki, Aoba-ku, Sendai, 980-8578, Japan

Jeffrey T. Freymueller

Geophysical Institute, University of Alaska Fairbanks, 903 Koyukuk Dr, Fairbanks, Ak 99775, United States

Volker Klemann

GFZ German Research Centre for Geosciences, Telegrafenberg, 14473 Potsdam, Germany

Abstract

Recent theoretical simulations on the Glacial isostatic adjustment (GIA) have revealed that the model differences arising from considering mantle compressibility are not necessarily negligible if compared with the observation accuracy of present-day deformation rates. In this study, a compressible model is constructed for the GIA in southeast Alaska, and the uplift rate is compared with GPS data and the incompressible case for the first time. It is shown that, for Maxwell rheology, the incompressible model potentially underestimates the mean uplift rate by approximately 27% (4 mm/yr) with respect to the compressible case and the difference is detectable given observational precision. This difference between the compressible and incompressible models is reduced to 10% by matching the flexural rigidity of both earth models. When carrying out an

*Corresponding author
Email address: y-tanaka@eri.u-tokyo.ac.jp (Yoshiyuki Tanaka*)

inversion using incompressible models, this adjustment is important to infer a physically more correct viscoelastic structure.

Keywords: GIA, postglacial rebound, GNSS, rheology, Alaska

1. Introduction

Ongoing uplift with rates amounting to 1 cm/yr have been observed in Northern America and Europe by geodetic measurements (e.g. Ekman and Mäkinen, 1996; Larsen et al., 2004; Sella et al., 2007). The uplift is considered to result from the deformation of the solid Earth caused by Glacial isostatic adjustment (GIA). Present-day deformation rates due to GIA have been theoretically estimated using physical models based on the viscoelastic response to space-time variations in surface ice sheet mass. In the models, the viscoelastic deformation is obtained by solving the governing equations including a quasi-static equation of motion and viscoelastic constitutive equations with boundary conditions for surface loading (Peltier, 1974). Different model factors have been considered to improve theoretical predictions, such as more general treatments of geometry of the modeling domain, inclusion of self-gravitational effects, more complex rheology, finer distributions of the density, elasticity and viscosity within the Earth (e.g. Spada et al., 2011). Using an inversion (Peltier, 1998), more important model factors and viscoelastic parameters such as the thickness of the lithosphere and the asthenospheric viscosity can be determined.

Of the model factors described above, the inclusion of compressibility is still a theoretical issue (Cambiotti et al. 2013). In the presence of compressibility, dilatation modes and instability modes appear, which cause numerical difficulties in calculating viscoelastic responses. Dilatation modes consist of a denumerably infinite set of eigenmodes. Various methods have been proposed to evaluate the dilatation modes (e.g. Fang and Hager, 1994; Hanyk et al., 1995; Vermeersen et al., 1996; Cambiotti et al. 2009; 2010a, b; Tanaka et al., 2009; 2011). Instability modes appear on timescales of orders of magnitude larger than that of the glaciation process when employing the density and elastic structure of PREM

(Dziewonski and Anderson, 1981; Vermeersen and Mitrovica, 2000). The instability occurs when the radial profile of the density and elasticity structure includes a portion which does not satisfy the Adams–William condition (Bullen, 1975; Plag and Jüttner, 1995). A first approach to avoid the instability is partly changing the radial profile so that it satisfies the above condition. However, a modified profile becomes inconsistent with the result of the seismic wave observation in PREM. A second approach is to consider that the linearized governing equations, in which the second-order terms are omitted, should be applied only up to time scales before the instability starts to grow (Vermeersen and Mitrovica, 2000). This practical view allows us to simulate the GIA process without the above inconsistency. However, in which manner the instability modes behave after a certain time within a non-linear theoretical framework has not been confirmed.

With the advance of computational power, the use of finite-element methods seems to have become more common in modeling GIA. The effects of compressibility are simulated in many studies employing such approaches (e.g. Geruo et al., 2012). Still, few studies have discussed the effects of compressibility on the basis of a comparison between a regional GIA model and actual observation data. Tanaka et al. (2011) estimated the effects of compressibility on the present-day global-scale deformation rates for PREM with Peltier (2004)'s ICE–5G (VM2) model, taking the above-mentioned second approach that does not remove the instability modes. They showed that the difference between the rates calculated for the compressible and incompressible cases was approximately 1–2 mm/yr in the polar regions. However, the result was not compared with observation data.

The largest present-day uplift rate considered to be driven by GIA is found in southeast Alaska, amounting to approximately 30 mm/yr (Larsen et al. 2004). The effects of compressibility are also expected to be the largest there. So far, the regional-scale GIA in southeast Alaska has been modeled for only the incompressible case (Section 2.3). In this short paper, the effects of compressibility on the GIA-induced vertical velocity field in southeast Alaska are investigated.

Using the method of Tanaka et al. (2011), the compressible case is modeled for a radially stratified, self-gravitating viscoelastic Earth. By comparing the result with the incompressible case obtained in a previous study, the detectability of the model differences is discussed. In this comparison, the necessity of the re-definition of the incompressible model is also emphasized. A more fundamental solution of the instability problem remains for future studies.

2. Model

2.1. Compressibility and flexural rigidity

Before modeling, the definition of the effects of compressibility in this study is clarified. In the following, the Maxwell rheology is adopted, which has been widely used in the modling of GIA. The constitutive law for the compressible case is represented as

$$\begin{aligned} \dot{\tau} &= \dot{\tau}^E - \frac{\mu}{\eta}\left(\tau - \frac{1}{3}\mathrm{tr}\tau\mathbf{I}\right), \\ \tau^E &= \lambda\left(\mathrm{div}\mathbf{u}\right)\mathbf{I} + 2\mu\epsilon, \\ \epsilon &= \frac{1}{2}\left(\mathrm{grad}\mathbf{u} + \mathrm{grad}^{\mathrm{T}}\mathbf{u}\right), \\ \frac{1}{3}\mathrm{tr}\tau &= K\mathrm{div}\mathbf{u} = \left(\lambda + \frac{2}{3}\mu\right)\mathrm{div}\mathbf{u} \end{aligned} \tag{1}$$

where τ and ϵ represent the stress and strain tensors, respectively, $\mathbf{u}$ denotes displacement, and λ, μ, K and η are Lamé's constants, the bulk modulus and the dynamic viscosity, respectively (Hanyk et al., 1995; Tanaka et al., 2011). The bulk modulus is frequency-independent, while the two Lamé's constants are frequency-dependent (see, eq. (7) in Peltier, 1974). In the compressible case, stress-induced density changes inside the Earth are allowed. In the incompressible case, the dilatation div$\mathbf{u}$ goes to zero (conservation of volume and density) and λ goes to infinity in such a way that the pressure increment ($\Pi = \lambda\mathrm{div}\mathbf{u}$) has a finite limit (Wu and Peltier, 1982).

Suppose that the density and viscoelasticity structure are given and the present-day uplift rates are calculated for the compressible and incompressible

cases, using the same Earth model. An inversion is not carried out. Then, the effects of compressibility can be simply evaluated by subtracting the rate for the incompressible case from that for the compressible case. This comparison will be performed in Section 3.1. As the given Earth model, the viscoelastic paramters determined with GPS data in southeast Alaska for the incompressible model (Sato et al., 2011) is employed.

Flexural rigidity (Lambeck and Nakiboglu, 1980) is also important when comparing compressible and incompressible models (see eq. (3) of Tanaka et al. (2009) for the definition). In the previous papers (Tanaka et al., 2009; 2011), it was revealed that the difference in the predicted rates for the two cases is greatly reducted when shear modulus and the thickness of the lithosphere in the incompressible Earth model is adjusted so that flexural rigidity becomes the same as in the compressible model. This means that a computational method assuming incompressibility can approximate the response of the compressible material by adjusting flexural rigidity. The adjustment also results in differences in the viscosity estimates through the changes in shear modulus and the thickness of the lithosphere. In order to decrease the differences in the viscosity estimates from the compressible case, the incompressible Earth model can be defined so that not shear modulus but flexural rigidity is the same as in the compressible model. In Section 3.2, a comparison focusing on this aspect will be presented.

2.2. GIA in southeast Alaska and the target of the modeling

Generally, the GIA stems from the variations in the ice sheet mass that started melting after three different periods: Last Glacial Maximum (LGM), Little Ice Age (LIA) and Present-Day (PD). The uplift being observed in southeast Alaska results mainly from the contributions of post-LIA and PD ice melting (Larsen et al., 2005; Sato et al., 2011, 2012). The distribution of uplift rates measured at 91 GPS sites is displayed in Fig. 1 of Sato et al. (2011). The rates range between 0.3–35 mm/yr with two peaks in the Yakutat Ice field and the central part of Glacier Bay. The mean uplift rate and the mean uncertainty over the 91 sites are 19.2 mm/yr and 2.3 mm/yr, respectively. In the following, only

the rebound due to post-LIA melting is modeled for the compressible case. The other contributions to the present-day rate may be ignored when discussing the effects of compressibility as explained below.

The uplift rate in southeast Alaska that originates from the Laurentide ice sheet after the LGM is less than 2 mm/yr (Sella et al., 2007 and Fig. 6 of Sato et al., 2011). Because the effects of compressibility on the load Love numbers are 10–40% (Tanaka et al., 2009), the difference due to the inclusion of compressibility becomes smaller than 1 mm/yr, which cannot be distinguished by the observation data with the uncertainty of 2.3 mm/yr. The contribution from the PD ice melting (PDIM) was modeled using ice height change data from the mid-1950s to the mid-1990s and illustrated in Fig. 3 of Sato et al. (2011). The largest rate in the model is 12 mm/yr around $139°W, 59.5°N$, which is not negligible, compared with the uncertainty. However, the deformation caused by the PDIM is modeled with an elastic deformation theory (e.g. Farrell, 1972). This means that the effect of compressibility is already considered in the elastic response. The vertical component of the tectonic motion is not significant in southeast Alaska and is neglected as in Larsen et al. (2005), Elliott et al. (2010) and Sato et al. (2012). The reference frame uncertainty and the load deformation caused by the secular sea level variation on the vertical velocity field can also be neglected (± 1 mm/yr and < 1 mm/yr, respectively) (Sato et al., 2011).

2.3. An overview of the modeling method

The present-day rate caused by post-LIA ice melting in southeast Alaska was modeled by Larsen et al. (2003, 2004, 2005) and Sato et al. (2011) for the incompressible case. The latter two studies constructed the rebound models with the TABOO software (Spada, 2003; Spada et al., 2003, 2004), which is based on a radially stratified, self-gravitating viscoelastic Earth. The viscoelastic structure in Sato et al. (2011) was constrained by the GPS data obtained at more observation sites than in Larsen et al. (2005). In the following, the compressible model is constructed in a manner which is as close as possible to the method described in section 4 of Sato et al. (2011), and is compared with

their incompressible model. In some studies, viscoelastic structures with lateral heterogeneities are considered in modeling the global-scale GIA (e.g. Klemann et al., 2008; Geruo et al., 2012). Still, estimating the effects in a 1-D case would be a necessary step before proceeding to investigating the effects in 3-D cases.

The spectral finite-element approach (Tanaka et al., 2011) is used for modeling the compressibile case. The governing equations are common to those used in TABOO except that volumetric change is allowed, which enables us to evaluate the difference arising only from the inclusion of compressibility. The relative accuracy of the numerical computation is considered to be better than a few per cent in estimating load Love numbers (Tanaka et al., 2011), which is at least an order of magnitude smaller than the expected effects of compressibility on the velocity field.

2.4. The viscoelastic structure

Sato et al. (2011) inferred the viscosity structure in southeast Alaska by inversion of GPS data. The inferred ranges of the thickness of the lithosphere and the viscosity in the upper mantle were 42–63 km and 3.0–13 $\times 10^{18}$ $Pa \cdot s$, respectively. The present-day rate is not sensitive to the viscosity in the lower mantle (Fig. 9 of Sato. et al., 2011), which is consistent with the fact that the theoretical model of Sato et al. (2011) considers the deformations with not only lower but also higher spherical harmonic degrees that correspond to the contributions from the shallower portion of the mantle (Section 2.6). The density and elastic constants were based on PREM. In our study, the optimum structure obtained in their inversion is employed (Table 1). Here, ρ, λ, μ and η denote the density, Lame's elastic constants, and viscosity, respectively. The parameters in each layer are volume averages of PREM. In the model of Sato et al. (2011), λ is replaced by infinity (Wu and Peltier, 1982). Hereafter, this structural model (and the result obtained by this model) is denoted as Model I (=Incompressible). In the compressible model (Model C (=Compressible)), λ shown in the table is used.

The effects of compressibility may vary with the definition of the incom-

pressible model as already mentioned. Tanaka et al. (2009, 2011) showed that the viscoelastic response to a surface load is governed by the flexural rigidity rather than the elastic constants. This implies that the effects of compressibility, in a physical sense, should be measured for models with the same flexural rigidity. In principle, the flexural rigidity in the incompressible model (Model I) should be adjusted as in Tanaka et al. (2009, 2011). However, this adjustment causes a discrepancy between Model I and the GPS data and an inversion using Model C is necessary. Our purpose, as a first step, is to estimate the effects of compressibility on regional GIA after the flexural rigidity is adjusted. This can be achieved by constructing another compressible model (Model CF) from Model C, where the flexural rigidity is the same as in Model I. This adjustment of Model C is a mathematical conversion, which may seem tricky. However, it is useful to obtain a theoretical estimate. To match the flexural rigidity, the elastic constants within the lithosphere and its thickness can be changed. Here, to reduce the freedom of the parameters, in Model CF, a relationship of $\lambda = \mu$ and the same lithospheric thickness as in Model I are assumed. Under these conditions, eq. (3) in Tanaka et al. (2009) yields that $\lambda = \mu = (3/2)\mu_{inc}$, where μ_{inc} denotes the rigidity in Model I. The result is shown in Table 1.

2.5. The ice load model

The same ice load model as in Sato et al. (2011) is used for the post-LIA period. The load model consists of five disks with diameters of 0.4° or 0.8° representing the Glacier Bay load and 531 disks with mean diameter 0.2° expressing the other regional glaciers and ice fields in southeast Alaska. The space-time distribution of the disk loads is shown in Fig. 5A of Larsen et al. (2005).

2.6. The calculation of the response to the loads

The viscoelastic relaxation is computed for spherical harmonic degrees $\leq$480 by the spectral finite-element approach for the 536 point loads. The same cut-off degree was used in Sato et al. (2011), which is enough to ensure convergence

of the spherical harmonics. The results are then converted into the responses to the disk loads with the disk factors of Farrell (1972). By superimposing the responses to the 536 disk loads, the vertical displacement rates in the year 2005.0 at 84 GPS observation sites are computed by a forward method. The rates at these sites were already used in the inversion for case B in Table 3 of Sato et al. (2011), which gave better agreement with the present-day ice melting model (UAF07). 7 sites included in case A of Sato et al. (2011), which were used for a comparison with the previous ice melting model (UAF05) and were located at latitude greater than 60°, were omitted.

3. Effects of compressibility

3.1. The case without the flexural rigidity adjusted

The rates computed with the method described above are compared with the vertical displacement rates shown in Fig. 1 (a). The rates are obtained by subtracting the contributions of the PDIM and the LGM (Fig. 1 (b)) from the above observation result. The effects of the PDIM and the LGM are those determined by the inversion in Sato et al. (2011). In Fig. 1 (b), the removed effect of the LGM is less than 2 mm/yr over the entire area as described before. Relatively large velocities seen in the northwestern part at latitude $\sim 59.5°$ reflect the effects of the PDIM (see Fig. 1 of Larsen et al. (2005) and Fig. 3 (b) of Sato et al. (2011)). Fig. 1 (a) shows that the residual rates at most sites distribute in the range of 10–20 mm/yr.

Fig. 2 shows comparisons between the rates in Fig. 1 (a) and the rates computed for Models I, C, and CF, respectively. A statistical analysis result for the differences between the observed rates and the models is shown in Fig. 3 and Table 2. Comparing Fig. 2 (a) and (b), the result of TABOO (=Model I) fits better with the observed rates than Model C. This is natural because the viscosity parameters were determined by the inversion so that the incompressible model explained the observation data. Fig. 2 (d) shows the residuals between the observation and the models. Compared with the white markers representing

Model I, the more black markers for the compressible case lie below the zero line, which implies that the predicted rates for the compressible model are larger than the observed ones. According to Table 2, the increase in the velocity is 3.8 mm/yr on average, which amounts to 27% of 14.7 mm/yr, which is the mean of the observed rates excluding the effects of the PDIM and the LGM. The amount and sense of the increase is consistent with results of previous theoretical studies (Hanyk et al., 1995; Tanaka et al., 2009, 2011). The difference of 3.8 mm/yr exceeds the average observation error with 2.3 mm/yr, indicating that the effect of compressibility, when measured with respect to the incompressible case without adjusting the flexural rigidity, is detectable by the GPS network.

The spatial pattern in the difference between Models I and C is displayed in Fig. 4 (a). From this figure and Fig. 3 (b), the differences in the rates at most sites lie between -5 and 0 mm/yr, resulting in a rather smooth spatial variation. This implies that, by increasing the viscosity in the asthenosphere by 27%, the difference of 3.8 mm/yr in the mean can be almost removed because a linear rheology (Maxwell) is assumed. The standard deviation for the compressible case (3.9 mm/yr) is slightly larger than for the incompressible case (3.3 mm/yr). The viscoelastic parameters employed here are optimized in the incompressible case by an inversion. Therefore, an inversion computation is necessary to confirm if the compressible model can explain the same observation data better.

3.2. The case with the flexural rigidity adjusted

Fig. 2 (c) shows the comparison of Model CF and the observation. As expected from the previous results, the difference between Models CF and I drastically decreases, and Model CF agrees with data better than Model C. The residual is plotted by grey data points in Fig. 2 (d). It can be seen that grey triangles become closer to the zero line. The average of the residuals is -1.4 mm/yr (Table 2). The difference of -1.4 mm amounts to 9.5% of the mean observed rate. Tanaka et al. (2009) mentioned that the rate of the load Love number for the compressible case is faster by approximately 10% for spherical degrees higher than 35, when comparing with that for the incompressible case

in which the flexural rigidity is adjusted (see section 5.2.1 and Fig. 4 (a) of the paper). This agrees with our result. The standard deviation of 3.4 mm/yr for Model CF is almost the same as 3.3 mm/yr for Model I (Table 2). As a result, the shape of the histogram becomes extremely similar to that of Model I (Fig. 3 (d)). This follows that, when increasing the viscosity in the asthenosphere by 9.5%, the difference of 1.4 mm/yr in the mean velocity is resolved, which makes it hard to discern the difference between Model I and Model CF by observation.

Fig. 4 (b) shows the spatial distribution of the misfits. As confirmed in the statistical analysis, the difference from the incompressible case is greatly reduced by adjusting the flexural rigidity (compare with Fig. 4 (a)). However, taking a closer look, the misfits are still relatively large in the northwestern area where the contribution of the PDIM is dominant (Fig. 5 of Larsen et al. (2005)). This is due to the fact that the uplift rate by the PDIM observed by GPS is so large in the Yakutat Ice Field that the rate computed by the model (UAF07) does not reproduce the contribution of the PDIM completely. A possible mechanism to explain the GIA process peculiar to Yakutat is discussed in Trüssel et al. (2013). In the other areas, the difference between Model I and Model CF almost disappears.

3.3. The ratio of gravity change rate to uplift rate

Using the method proposed by Wahr et al. (1995), Sato et al. (2012) calculated the ratio of the gravity change rate to the uplift rate to discuss the present-day ice thickness changes. The effects of compressibility on the ratio can be theoretically estimated by computing the ratios for Models I, C, and CF. Table 3 shows the result. The differences between I and C and I and CF are 4×10^{-4} and 1×10^{-4} μGal/mm, respectively, which are well below the standard deviation of 1×10^{-3} μGal/mm. Considering that the standard deviation for the fitting residuals against the observed gravity change and uplift rates was 0.052 μGal/mm (Sato et al., 2012), the effects of compressibility on the ratio are negligible.

3.4. The horizontal velocity field

In the present study, the horizontal velocity field was not modeled. Horizontal rates in the study area observed by GPS are shown and interpreted in Freymueller et al. (2008) and Elliott et al. (2010). The rates range from a few mm/yr to 40 mm/yr, and the variation is mainly due to tectonic block motion. The GIA-induced horizontal displacement rate estimated by TABOO is shown in Fig. 3 of Elliott et al. (2010). The rates across Glacier Bay are 0.5–3 mm/yr. It follows that expected effects of compressibility on the horizontal component would be at most approximately 1 mm/yr, considering the effects on the load Love number for the horizontal component (Tanaka et al., 2009). To identify the difference of 1 mm/yr as the effects of compressibility in the above observed velocity field seems a challenge, considering the uncertainty of the reference frame (1 mm/yr), the observation errors (1–2 mm/yr), and the modeling uncertainties of the block motion (1–2 mm /yr) (Elliott et al., 2010).

4. Conclusions

The vertical displacement field in southeast Alaska caused by the glacial rebound due to the post-LIA melting was modeled. For the compressible case, the method of Tanaka et al. (2011) was applied to a spherically symmetric, self-gravitating Maxwell viscoelastic Earth model. For the incompressible case, the TABOO software was used. The difference between the governing equations for the two cases is the permission of volumetric change only. So, by comparing the computed results obtained by both methods, the effects of compressibility were estimated.

The computed result showed that the present-day uplift rate was faster by approximately 27% (4 mm/yr) in the compressible case. This increase in the rate was larger than the observation uncertainty of 2.3 mm/yr. This means that the viscosity in the asthenosphere determined using the incompressible model is underestimated by 27% when the same shear modulus and lithospheric thickness as in the compressible model is used in an inversion.

However, by matching the flexural rigidity in the compressible model with that in the incompressible model, the difference in the uplift rates was reduced to 10% (=1.4 mm/yr). To match the flexural rigidity, the shear modulus and/or the thickness of the lithosphere can be modified. In this study, only the former was changed for computational convenience. However, when the elastic structure is constrained by regional seismic wave observations, only the latter should be modified. This result associated with the adjustment of flexural rigidity implies that the definition of the incompressible model can affect inferences of the lithospheric thickness and the asthenospheric viscosity. To obtain a physically more correct viscosity structure using an incompressible model, the incompressible case should be re-defined so that its flexural rigidity is the same as in the compressible model. The last conclusion was derived by maintaining the fit between the incompressible model and the GPS data, and the internal viscosity structure for the compressible case has not yet been determined. To infer it by an inversion with the compressible model is left for a future study.

Tanaka et al. (2011) pointed out that the effects of compressibility on lower-harmonic-degree deformations with wavelengths longer than 8,000 km remain even when the flexural rigidity is adjusted (Fig. 8 of their paper). If adopting the above definition of the incompressible case, the inclusion of compressibility may be more important in a global-scale GIA modeling than in a regional-scale one.

Acknowledgements

The manuscript was greatly improved by the comments from the two anonymous reviewers. This work was partly supported by JSPS KAKENHI Grant Number 17253003.

References

Bullen, K. E., 1975. The Earth's Density. Chapman and Hall, London, 420 pp.

Cambiotti, G., Barletta, V. R., Bordoni, A. and Sabadini, R., 2009. A comparative analysis of the solutions for a Maxwell Earth: the role of the advection and buoyancy force, Geophys. J. Int., 176, 995–1006.

Cambiotti, G. and Sabadini, R., 2010a. The compressional and compositional stratifications in Maxwell earth models: the gravitational overturning and the long-period tangential flux, Geophys. J. Int., 180, 475– 500.

Cambiotti, G., Ricard, Y. and Sabadini, R., 2010b. Ice age True Polar Wander in a compressible and non-hydrostatic Earth Geophys. J. Int., 183, 1248–1264.

Cambiotti, G., Klemann, V. and R. Sabadini, 2013. Compressible viscoelastodynamics of a spherical body at long timescales and its isostatic equilibrium, Geophys. J. Int., 193, 1071–1082.

Dziewonski, A. M. and Anderson, A., 1981. Preliminary reference earth model, Phys. Earth planet. Inter., 25, 297–356.

Ekman, M. and Mäkinen, J. 1996. Recent postglacial rebound, gravity change and mantle flow in Fennoscandia, Geophys. J. Int. 126, 229–234.

Elliott, J. L., Larsen, C. F., Freymueller, J. T. and Motyka, R. J., 2010. Tectonic block motion and glacial isostatic adjustment in southeast Alaska and adjacent Canada constrained by GPS measurements, J. Geophys. Res., 115, B09407, doi:10.1029/2009JB007139.

Fang, M. and Hager, B. H., 1994. A singularity free approch to postglacial rebound calculations, Geophys. Res. Lett. 21, 2131–2134.

Farrell, W. E., 1972. Deformation of the Earth by Surface Loads, Rev. Geophys., 10, 761–797.

Freymueller, J. T., Woodard, H., Cohen, S., Cross, R., Elliott, J., Larsen, C., Hreinsdottir, S. and Zweck C., 2008. Active deformation processes in Alaska, based on 15 years of GPS measurements, in Active Tectonics and Seismic Potential of Alaska, AGU Geophysical Monograph, 179, Freymueller, J. T., Haeussler, P. J., Wesson, R. and Ekstrom, G., eds., pp. 1–42, AGU, Washington, D.C.

Geruo, A., Wahr, J. and Zhong, S., 2012. Computations of the viscoelastic response of a 3-D compressible Earth to surface loading: an application to

Glacial Isostatic Adjustment in Antarctica and Canada, Geophys. J. Int. 192, 557–572.

Klemann, V., Martinec, Z. and Ivins, E. R., 2008. Glacial isostasy and plate motion, J. Geodyn., 46, 95–103.

Lambeck, K. and Nakiboglu, S. M., 1980. Seamount loading and stress in the ocean lithosphere, J. Geophys. Res. 85, 6403–6418.

Larsen, C. F., Echelmeyer, K. A., Freymueller, J. T., Motyka, R. J., 2003. Tide gauge records of uplift along the northern Pacific-North American plate boundary, 1937 to 2001, J. Geophys. Res. 108, 2216, doi:10.1029/2001JB001685.

Larsen, C. F., Motyka, R.J., Freymueller, J. T., Echelmeyer, K. A., and Ivins, E. R., 2004. Rapid uplift of southern Alaska caused by recent ice loss, Geophys. J. Int., 158, 1118–1133.

Larsen, C. F., Motyka, R.J., Freymueller, J. T., Echelmeyer, K. A., and Ivins, E. R., 2005. Rapid viscoelastic uplift in southeast Alaska caused by post-Little Ice Age glacial retreat, Earth and Planetary Sci. Lett. 237, 548–560.

Peltier, W. R., 1974. The impulse response of a Maxwell Earth, Rev. Geophys. Space. Phys., 12, 649–669.

Peltier, W. R., 1998. Postglacial variations in the level of the sea: implications for climate dynamics and solid-Earth geophysics, Rev. Geophys., 36, 603–689.

Peltier, W. R., 2004. Global glacial isostasy and the surface of the ice-age Earth: the ICE–5G (VM2) model and GRACE, Ann. Rev. Earth Planet. Sci., 32, 111–149.

Sato, T., Larsen, C. F., Miura, S., Ohta, Y., Fujimoto, H., Sun, W., Motyka, R. J. and Freymueller, J. T., 2011. Reevaluation of the viscoelastic and elastic responses to the past and present-day ice changes in Southeast Alaska, Tectonophysics, 511, 79–88.

Sato, T., Miura, S., Sun, W., Sugano, T., Freymueller, J. T., Larsen, C. F., Ohta, Y. Fujimoto, H., Inazu, D., and Motyka, R. J., 2012. Gravity and uplift rates observed in southeast Alaska and their comparison with GIA model predictions, J. Geophys. Res., 117, B01401, doi:10.1029/2011JB008485.

Sella, G. F., Stein, S. Dixon, T. H., Craymer, M. James, T. S., Mazzotti, S., and Dokka, R. K., 2007. Observation of glacial isostatic adjustment in stable North America with GPS, Geophys. Res. Lett., 34, L02306, doi:10.1029/2006GL027081.

Spada, G., 2003. The Theory Behind TABOO. Samizdat Press, Golden-White River Junction.

Spada, G., Antonioli, A., Boschi, L., Brandi, V., Cianetti, S., Galvani, G., Giunchi, C., Perniola, B., Piana, N., Piersanti, A., Agostinetti, Stocchi, P., 2003. TABOO, User Guide., Samizdat Press, Golden-White River Junction.

Spada, G., Antonioli, A., Boschi, L., Brandi, V., Cianetti, S., Galvani, G., Giunchi, C., Perniola, B., Agostinetti, N.P., Piersanti, A., Stocchi, P., 2004. Geodesy: modeling earth's post-glacial rebound. Eos Trans. AGU 85 (6), 62.

Spada, G., Barletta, V. R., Klemann, V., Riva, R. E. M., Martinec, Z., Gasperini, P., Lund, B., Wolf, D., Vermeersen, L. L. A., and King, M. A., 2011. A benchmark study for glacial isostatic adjustment codes, Geophys. J. Int., 185, 106–132.

Tanaka, Y., Klemann, V., and Okuno, J., 2009. Application of a numerical inverse Laplace integration method to surface loading on a viscoelastic compressible Earth model, Pure. Appl. Geophys., 166, 1199–1216.

Tanaka,Y., V. Klemann, Z. Martinec and R. E. M. Riva, 2011. Spectral-finite element approach to viscoelastic relaxation in a spherical compressible Earth: application to GIA modelling, Geophys. J. Int., 184, 220–234.

Trüssel, B. L., Motyka, R. J., Truffer, M., and Larsen C. F., 2013. Rapid thinning of lake-calving Yakutat Glacier and the collapse of the Yakutat Icefield, southeast Alaska, USA, J. Glaciology, 59, doi:10.3189/2013J0G12J081

Vermeersen, L. L. A., Sabadini, R., and Spada, G., 1996. Compressible rotational deformation, Geophys. J. Int., 126, 735–761.

Vermeersen, L. L. A., and Mitrovica, J.X., 2000. Gravitational stability of spherical self-gravitating relaxation models, Geophys. J. Int., 142, 351–360.

Wahr, J., DaZhong, H., and Trupin, A., 1995. Predictions of vertical uplift caused by changing polar ice volumes on a viscoelastic Earth, Geophys. Res.

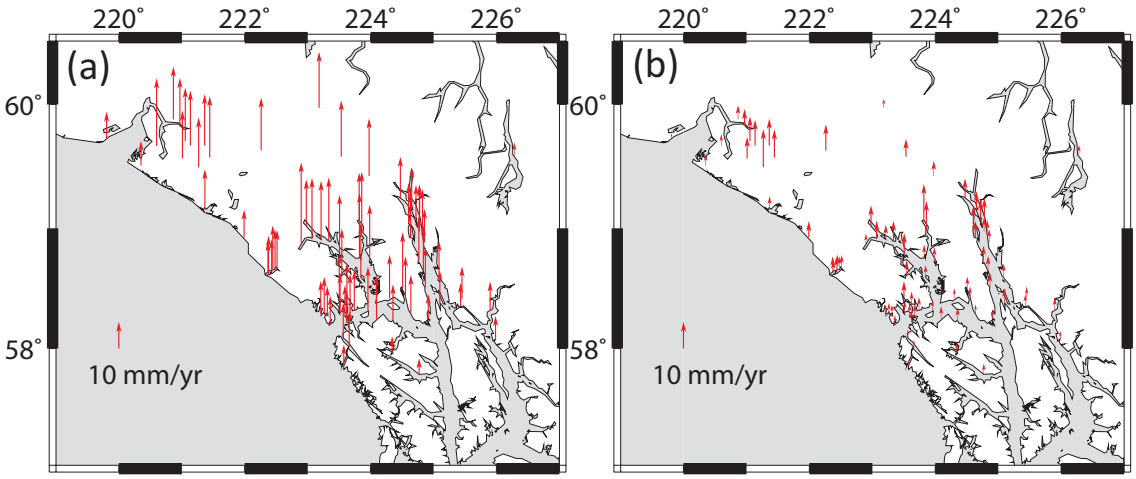

Figure 1: (a) The observed displacement rates. The effects of the PD and post-LGM are subtracted in advance to show the contribution of the post-LIA. The error bars are shown in Fig. 2. (b) The rates for the PDIM and LGM that were theoretically estimated in Sato et al. (2010).

Lett., 22, 977–980, doi:10.1029/94GL02840.

Wu, P., and Peltier, W. R., 1982. Viscous gravitational relaxation, Geophys. J. R. astr. Soc. 70, 435–485

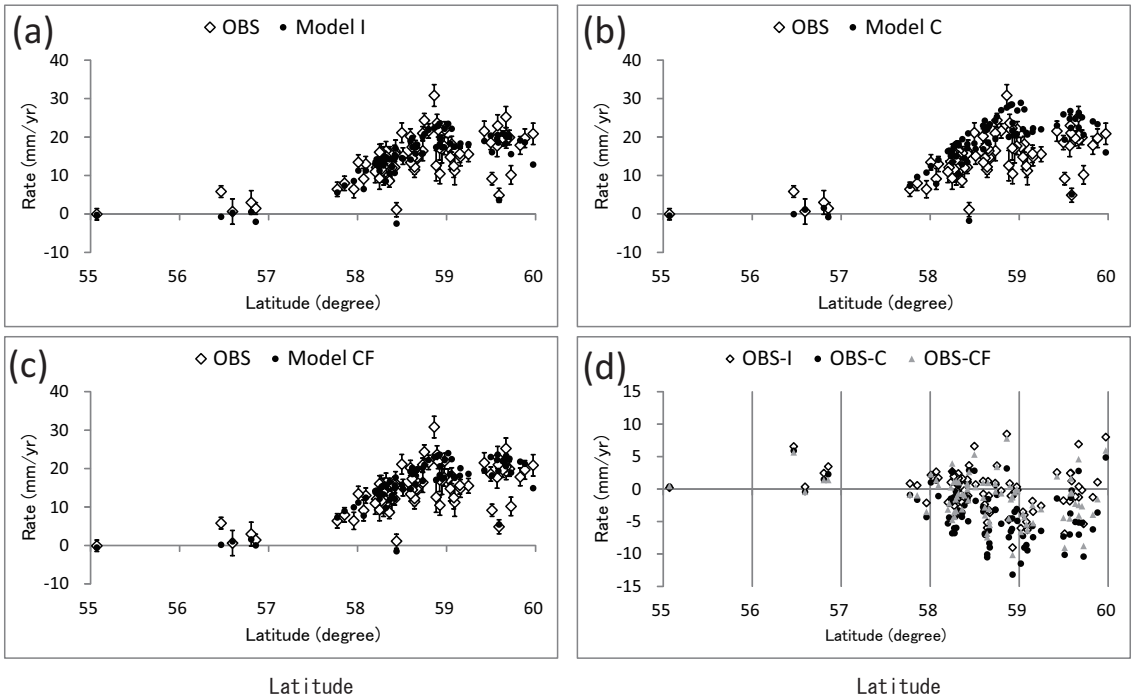

Figure 2: Comparisons between the observation and Models I (a), C (b), and CF (c). The horizontal and vertical axes denote the vertical velocity in mm/yr and latitude in degree, respectively. The white markers with error bars in (a–c) represent the observation result (Fig. 1 (a)). The differences between the observation and the models are plotted in (d).

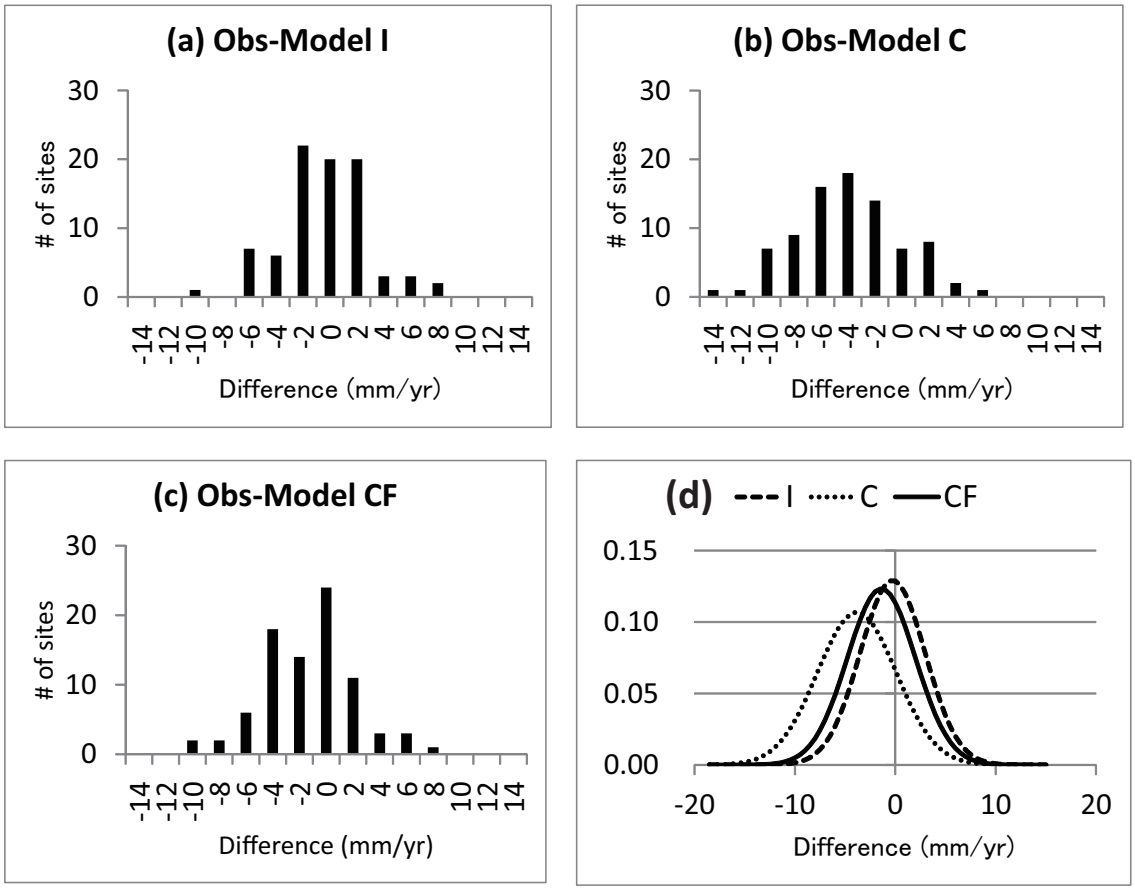

Figure 3: (a–c) The histograms of the residuals in Fig. 2 (d). The vertical axes denote the number of data. (d) The normal distributions corresponding to the average and the standard deviation for the three cases (see also Table 2). The vertical axis denotes the probability density.

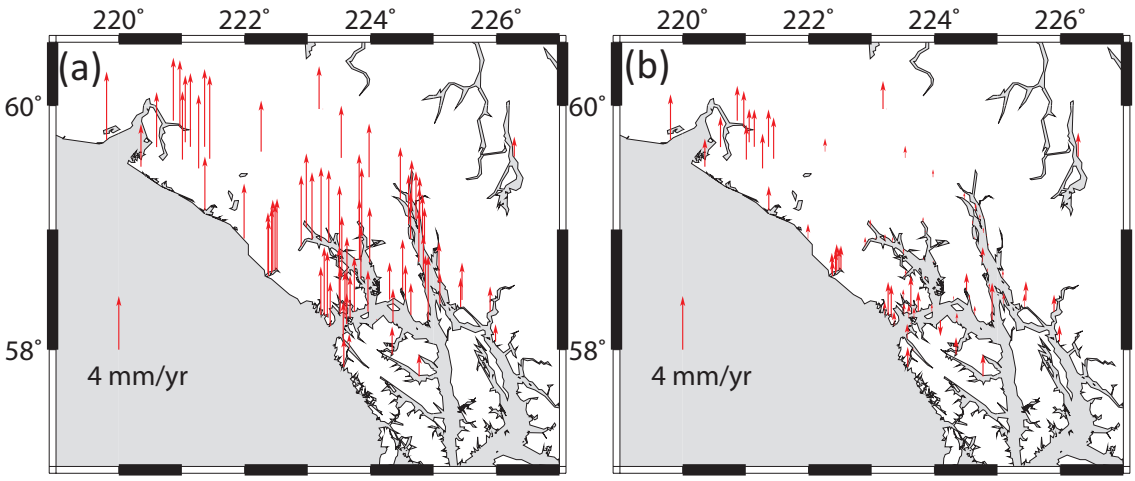

Figure 4: The spatial distributions of the differences of the compressible models with respect to the incompressible model. (a) Model C-Model I and (b) Model CF-Model I. Note that the scale of the rates is different from that in Fig. 1.

Table 1: The viscoelastic structures used in the modeling. $\rho(r)$, $\mu(r)$, and $\eta(r)$ in layer 1–6, representing the values for $R_1 \leq r \leq R_2$, where r is the radius, agree with the optimum parameters of Sato et al. (2010). λ is computed by the volume average of PREM as for the density and the rigidity. In Model CF, where the flexural rigidity is adjusted, the elastic constants within the lithosphere are replaced with those shown in the last raw.

Layer	R_1 (km)	R_2 (km)	ρ (kg/m^3)	λ (GPa)	μ (GPa)	η (Pa·s)
1	0	3480	10.93	-	-	-
2	3480	5701	4.88	344	219	2×10^{21}
3	5701	5971	3.86	146	107	4×10^{20}
4	5971	6151	3.48	111	76.5	4×10^{20}
5	6151	6311	3.37	77.0	66.8	10^{19}
6	6311	6371	3.03	62.3	52.5	-
6 (CF)	6311	6371	3.03	78.8	78.8	-

Table 2: The average and the standard deviation for the difference between the observation and the model for the three cases. The number of data is 84. The same data are shown in Fig. 2 (d) and Fig. 3 (a–c).

Case	Ave. (mm/yr)	S.D. (mm/yr)
Obs-Model I	-0.3	3.3
Obs-Model C	-3.8	3.9
Obs-Model CF	-1.4	3.4

Table 3: The result for a linear regression agains the ratio of gravity change rate to uplift rate. The rates are estimated at 2005.0 over the 84 sites for the shown three models.

Model	Ratio (μGal/mm)	S.D. (μGal/mm)
I	-0.1725	0.001
C	-0.1729	0.001
CF	-0.1726	0.001

LaTex Source Files

Click here to download LaTeX Source Files: JGEODYN-rev2.tex

Figure1

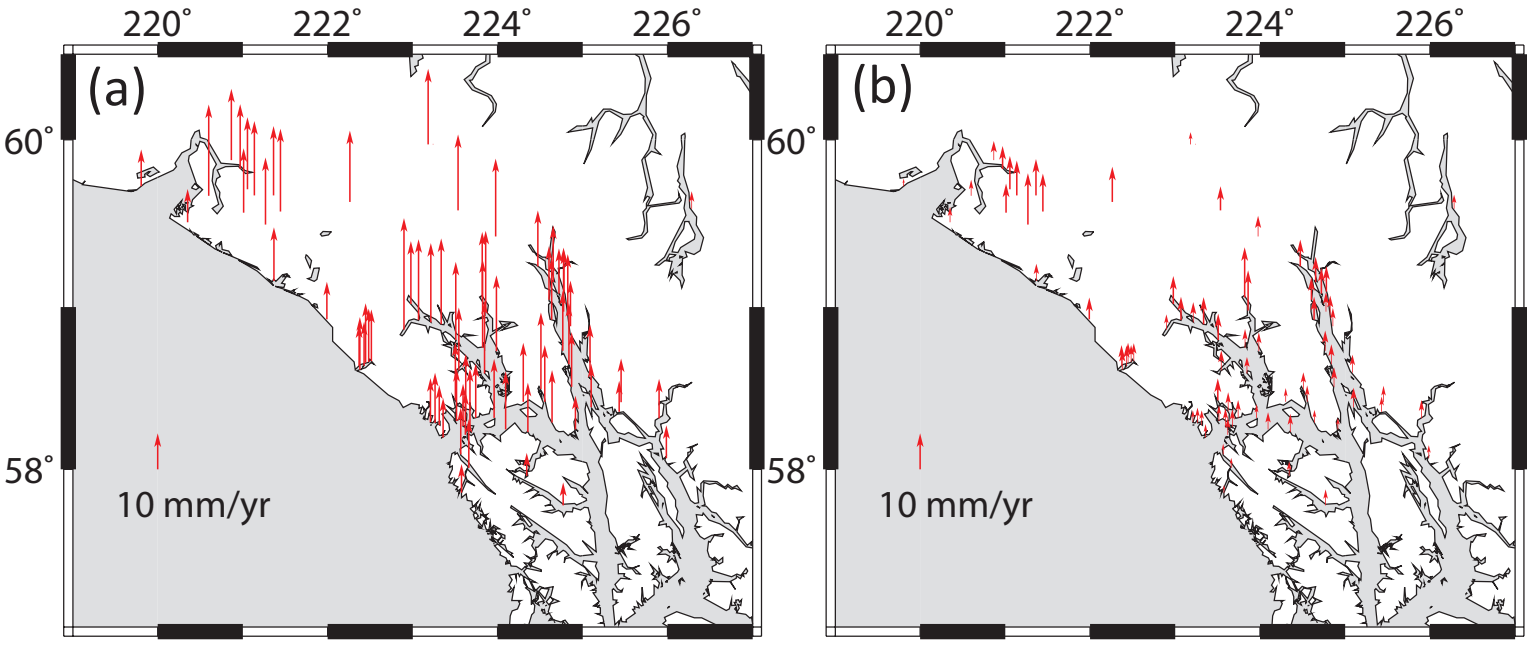

Figure2

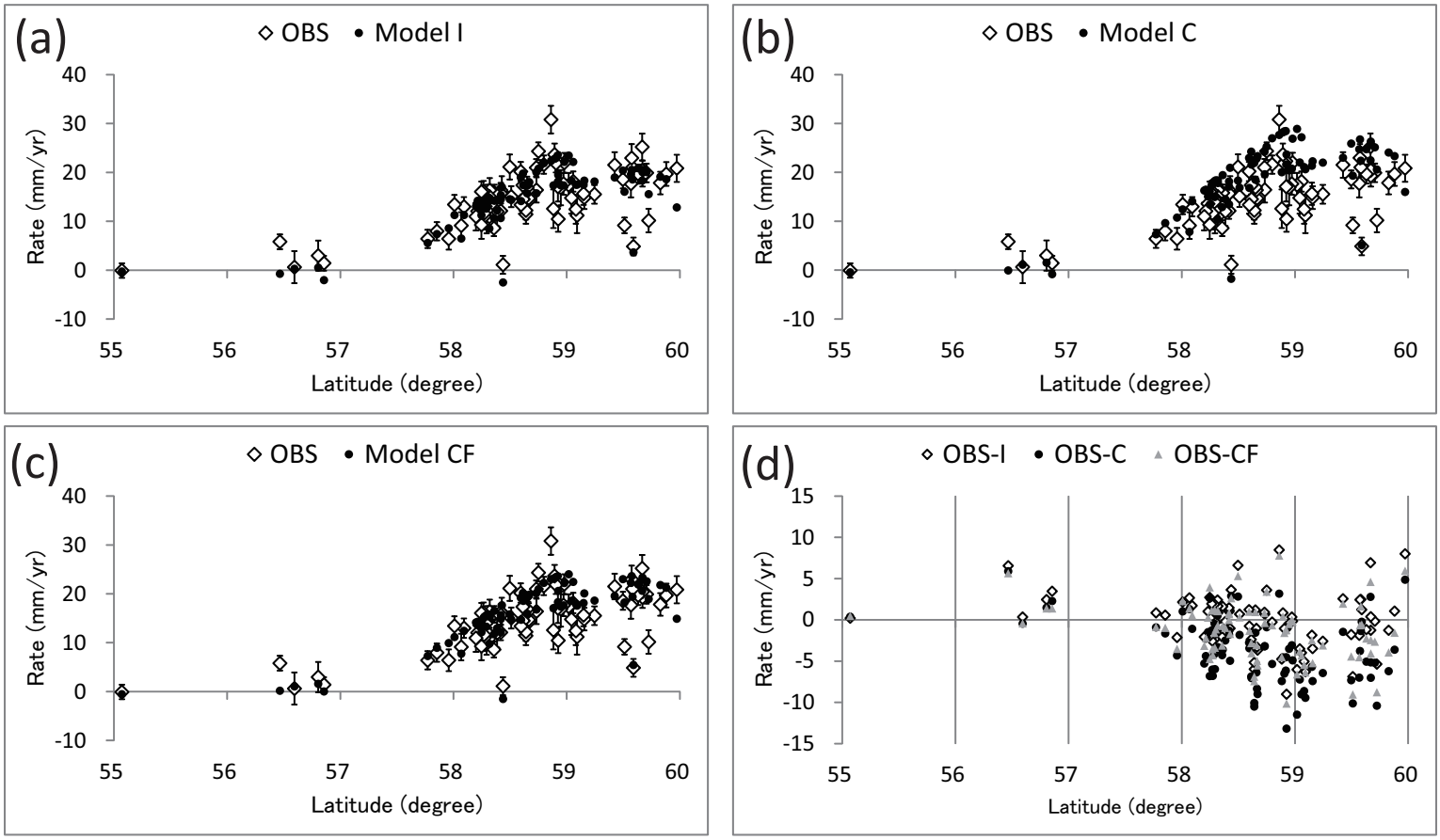

Latitude

Latitude

Figure3

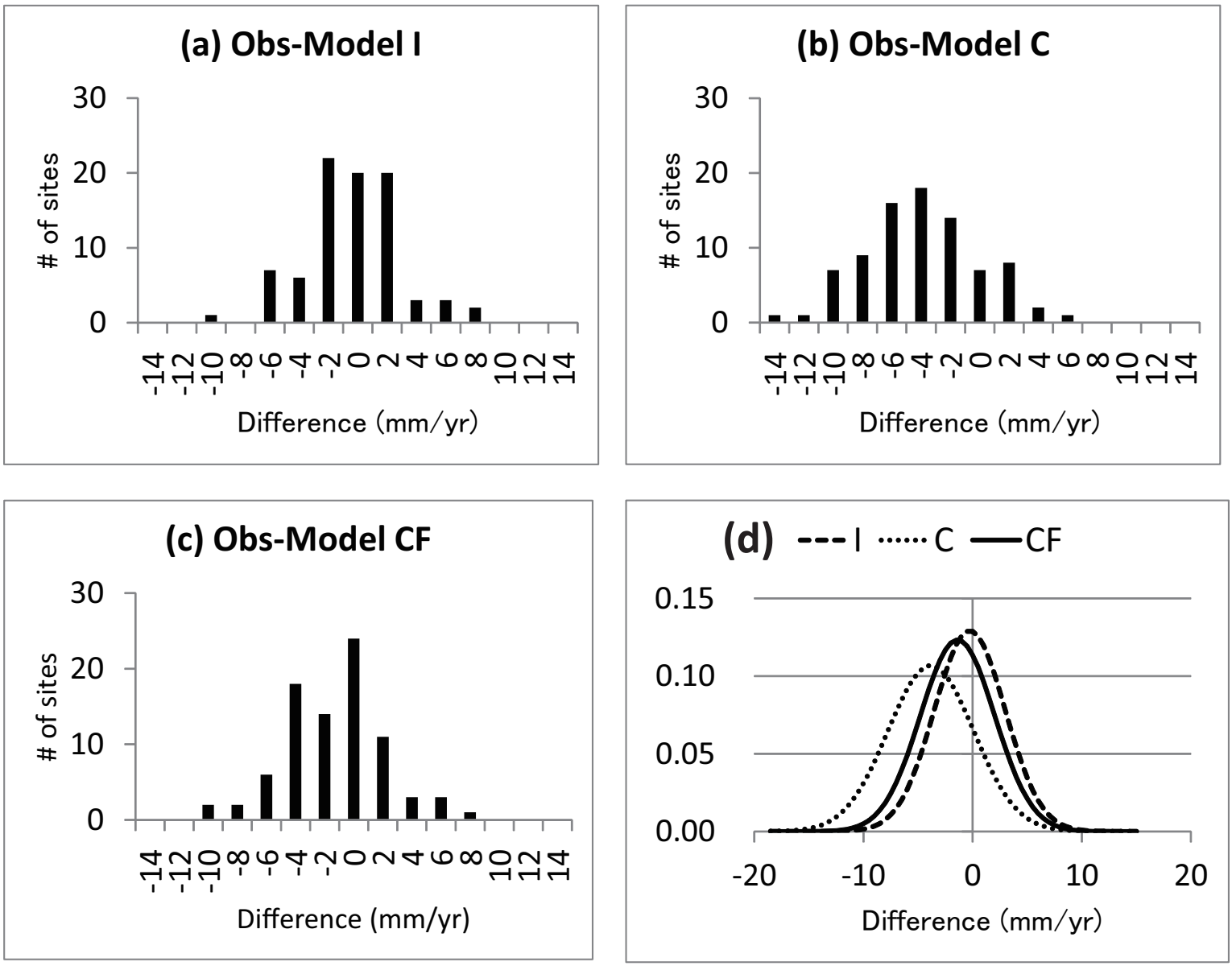
(a) Obs-Model I
# of sites
Difference (mm/yr)
(b) Obs-Model C
# of sites
Difference (mm/yr)
(c) Obs-Model CF
# of sites
Difference (mm/yr)
(d)
I
C
CF
Difference (mm/yr)

Figure4

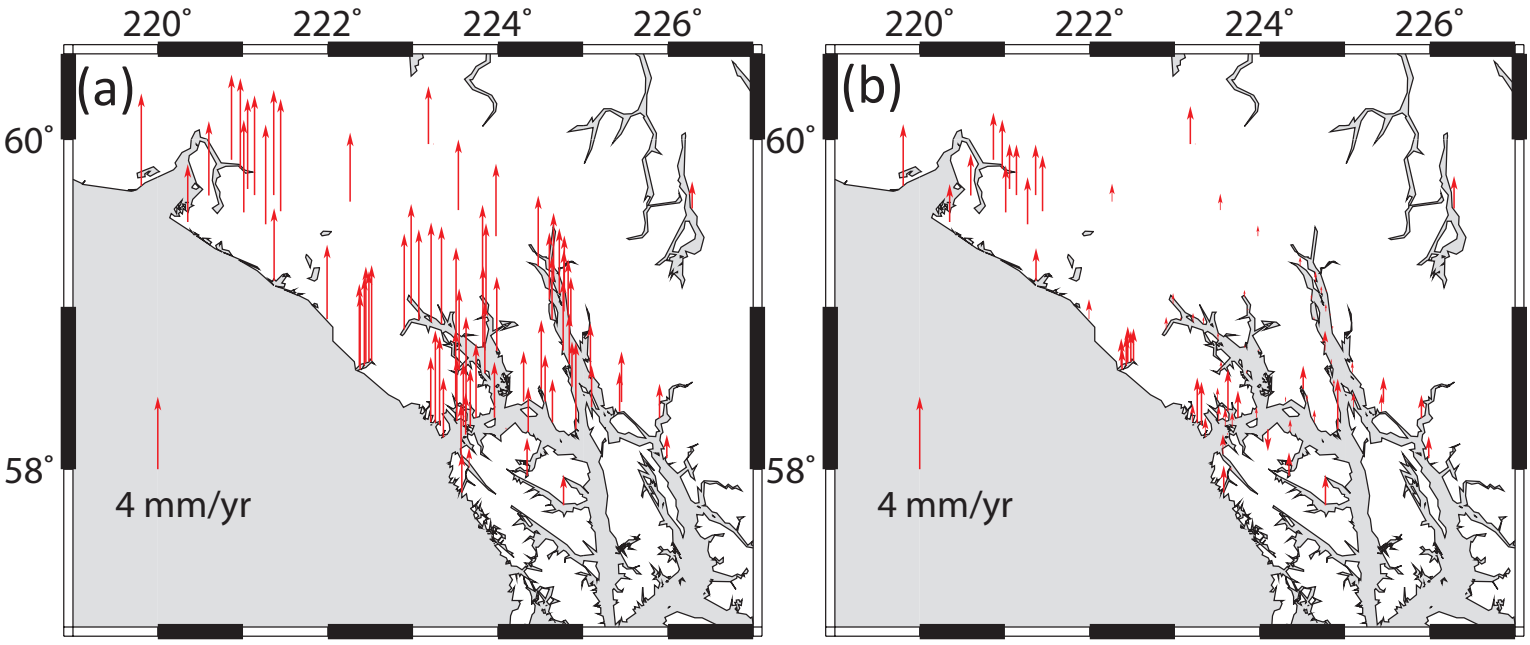

manuscript where changes are highlighted
Click here to download Supplementary data (e-component): JGEODYN-rev2_highlighted.pdf